Effect of organic electroactive crystallites in a dielectric matrix on the electrical properties of a polymer dielectric

Taein Lee,[1] Yue Luo,[2] Chuhong Wang,[1] Abigail Park,[1] Elmer Zapata-Mercado,[1] Kalina Hristova,[1] Timothy Mueller,[1] William L. Wilson,[2] Daniel H. Reich,[3] and Howard E. Katz[1]

[1]*Department of Materials Science and Engineering, Johns Hopkins University, 3400 North Charles Street, Baltimore, Maryland 21218, USA*
[2]*Center for Nanoscale Systems, Harvard University, 11 Oxford Street, Cambridge, Massachusetts 02138, USA*
[3]*Department of Physics and Astronomy, Johns Hopkins University, 3400 North Charles Street, Baltimore, Maryland 21218, USA*

(Received 25 January 2023; revised 18 May 2023; accepted 22 May 2023; published 30 June 2023)

The effects of inserting chargeable α-quaterthiophene ($\alpha 4T$) crystallites in polystyrene (PS) multilayers used as a transistor gate and capacitor dielectric were investigated. X-ray diffraction, scanning electron microscopy with energy-dispersive x-ray spectroscopy, and confocal microscopy indicated the formation of $\alpha 4T$ crystallites in the PS matrix. A modified saturation-regime current-voltage relationship was used to estimate organic field-effect transistor (OFET) threshold voltage V_{TH} shifting, and in turn the quantities of stored charge that were observed as a result of dielectric charging. The crystallites increased the maximum charge-storage capacity as well as the charge-retention capability of the dielectrics. Kelvin probe force microscopy showed that charges were localized near the $\alpha 4T$ crystallites upon charging. Trilayer experiments validated the charge-retention improvement of $\alpha 4T$ crystallite-embedded PS dielectrics. The crystallites also improved breakdown characteristics in PS used as a capacitor dielectric, suggesting their application to storage capacitors in addition to OFET logic.

DOI: 10.1103/PhysRevMaterials.7.065003

I. INTRODUCTION

Field-effect transistors (FETs) are circuit elements that can be incorporated into logic systems or amplify and switch electrical signals. They are the primary building blocks of modern electronics. Beginning a few decades ago, the functions and capabilities of traditional metal-oxide-semiconductor field-effect transistors have expanded through active research in organic field-effect transistors (OFETs), which provide ease of molecular design, low cost, light weight, flexibility, and solution processability [1–5].

Among the components of FET or OFET devices, dielectric layers have been widely investigated for their influence on FET performance via surface modification for favorable interfacial properties and/or for their charge-trapping functionalities [6–8]. However, compared to research on organic alternatives for other components in transistors, research on organic dielectrics has been relatively less emphasized [6,9]. Surfaces of silicon oxide dielectric layers were modified to enhance performance of organic semiconductor (OSC) charge mobilities via self-assembled monolayers on gate dielectrics or to provide surface functionalization for electrical sensors [10,11]. In a more direct application of organic dielectrics, organic polymers and copolymers have been investigated systematically based on the theory of percolative nanocomposite additives to increase the energy density of dielectrics for applications in capacitors or other forms of energy storage [12–14].

Another aspect of dielectrics as active materials includes the ability to control threshold gate voltage (V_{TH}, related to the onset of channel current) shifts in OFETs by trapping injected charge, also known as bias stress effects [5,7]. We have previously controlled pentacene OFET V_{TH} shifts by trapping injected charge in synthesized polystyrene (PS)-based gate dielectrics containing electroactive molecular subunits [15–19]. In the present paper, we report the embedding of electroactive organic *crystallites* based on aggregating molecules in PS dielectric materials (relative permittivity of 2.4–2.7 from standard references and handbooks) and their incorporation into pentacene OFETs to investigate the effects of these aggregates on charge-storage behavior and on the resilience of gate dielectrics.

Quaterthiophene ($\alpha 4T$) was chosen for the electroactive crystallites because of its ready formation of crystals from solution, low but finite solubility in ordinary organic solvents, and environmental stability [20–24]. We analyzed the charge-trapping properties of $\alpha 4T$ crystallite-embedded PS dielectrics in OFETs and in stand-alone PS films. The structures of the crystallite-embedded films were analyzed using x-ray diffraction (XRD) to determine the existence of crystalline $\alpha 4T$. Three-dimensional laser optical microscopy, scanning electron microscopy (SEM) with energy-dispersive x-ray spectroscopy (EDS), and confocal microscopy were used to investigate the size and shape of the embedded $\alpha 4T$ crystallites. Kelvin probe force microscopy (KPFM) enabled us to observe localization of stored charge near the $\alpha 4T$ crystallites.

OFET V_{TH} shifts were used to investigate the influence of the $\alpha 4T$ crystallites on the maximum charge-storage capacity and charge-retention capability of the films. Varying the position of the $\alpha 4T$ crystallite-embedded layer in bilayer and trilayer dielectrics validated the activity of the crystallites as charge-storing entities, above and beyond the PS, and revealed differences in charging response depending on the charge-injecting interfaces. Density-functional theory (DFT)

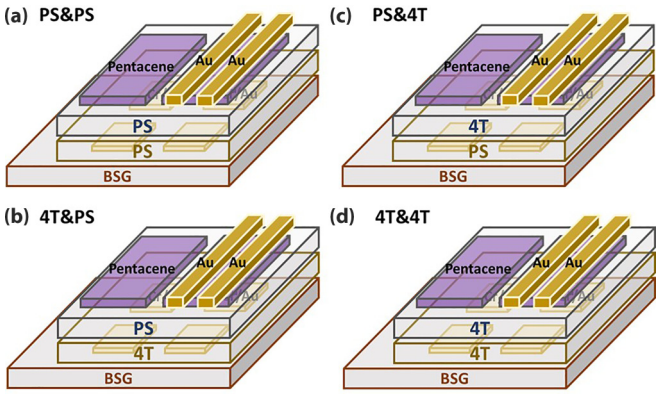

FIG. 1. Schematic of OFETs with (a) PS&PS dielectric, (b) PS&4T dielectric, (c) 4T&PS dielectric, and (d) 4T&4T dielectric. Lower shadowed gold rectangular prisms indicate gate pads under the lower dielectric layer. Violet rectangular prisms indicate pentacene, on which top gold source and drain electrodes are shown for illustration purposes on the right-hand pentacene features, although they are present on all pentacene films.

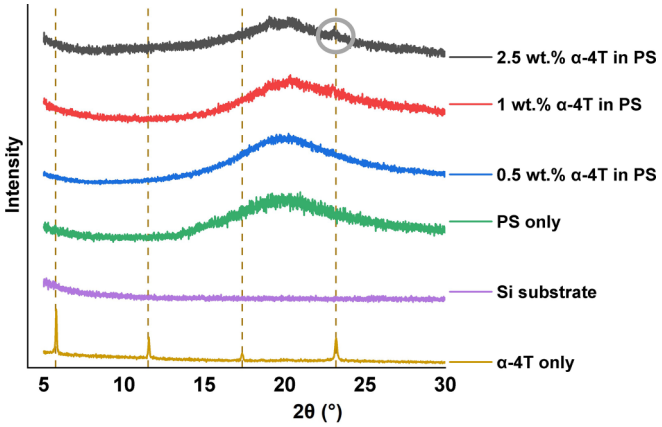

FIG. 2. Intensity vs. scattering angle 2θ for XRD of 2.5, 1, and 0.5 wt. % $\alpha 4T$ in PS, PS only, Si only, and $\alpha 4T$ only. The first sign of a small $\alpha 4T$ peak at 1 wt. % $\alpha 4T$ in PS is indicated.

calculations further supported the hypothesis that molecular crystallites could stabilize static charge better than would the same molecules in isolation. We additionally found that these crystallites can also decrease dielectric breakdown of PS dielectrics in capacitors.

II. EXPERIMENT

Detailed experimental procedures, material sources, and instrument specifications are provided in the Supplemental Material (SM). Briefly, polystyrene was spin coated from 20 wt. % solutions in tetrahydrofuran. Both stand-alone dielectric films and OFETs were fabricated on borosilicate glass (BSG) substrates. Gold electrodes and pentacene semiconductor layers were vapor deposited. Single dielectric layers, four types of dielectric bilayers (Fig. 1), and trilayers were explored, with the $\alpha 4T$ in either the top or bottom layers or both in bilayers, and in the middle of a trilayers. The bilayers are denoted as PS&PS, PS&4T, 4T&PS, and 4T&4T (Fig. 1). A modified method for determining the V_{TH} shift was developed and is also described in the SM. This method parametrized the shift of transfer curves without relying on an exact numerical designation for V_{TH} itself.

III. RESULTS AND DISCUSSION

A. DFT calculations

Further motivation for using a π-conjugated oligomer crystallite as a charge-storing additive came from electronic modeling of modest-sized aggregates. DFT calculations were performed to study the electronic structures of the electroactive molecules in the gas phase as well as in polystyrene considered as the solvent. Molecular structures were optimized by DFT methods at the PW6B95-D3/def2-QZVPP level of theory [25,26] using the ORCA software package [27]. The solution phase was implicitly modeled using the conductor-like polarizable continuum model [28].

We determined the ionization energy by calculating the difference between the energies in the neutral and positive state. We chose 5-hexyl-2,2′:5′,2″:5″,2‴-α-quaterthiophene to represent $\alpha 4T$ in close proximity (or possibly attached) to a hydrocarbon backbone and that would be in an enforced parallel alignment as an aggregate. Its ionization potential evolved from 6.4 eV as a gas-phase molecule to 5.5 eV in polystyrene solvent to 5.2 and 4.9 eV as four-molecule structure-optimized parallel arrays in gas phase and polystyrene, respectively. This supports the proposition that aggregated molecules such as $\alpha 4T$ could have greater charge-storing capability than would isolated molecular subunits, even in a solvent consisting largely of alkylbenzene rings. Analogous trends were observed when modeling 2-diethylaminoanthracene and "6,13-Bis(tripropylsilylethynl)pentacene (TIPS-pentacene)," which also crystallize from nonpolar media and have similar electron-donating capabilities [29].

B. Dielectric characterization

The morphology and chemical composition of the devices were characterized using 3D laser optical microscopy to determine the surface roughness, XRD to identify and prove the presence of $\alpha 4T$ crystallites in the PS dielectric matrix, and SEM/EDS as well as confocal microscopy to specifically locate $\alpha 4T$ crystallites on the surface of the $\alpha 4T$ crystallite embedded PS dielectric matrix.

Figure 2 shows that 2.5 wt. % $\alpha 4T$ is a borderline concentration in PS at which the $\alpha 4T$ peak at scattering angle $2\theta = 23^{\circ}$ is visible compared to the neat powder, while it is marginal in the 1% sample. There was significant masking of the $\alpha 4T$ XRD signal from the amorphous peak of the PS. However, as our objective was to fabricate PS dielectrics with the smallest observable nanocrystals of $\alpha 4T$ embedded in it, 1 wt. % $\alpha 4T$ in PS was chosen as the $\alpha 4T$ composition in the PS dielectric.

Figure 3 shows images taken by the 3D laser optical microscope at 50 × magnification. Figures 3(a) and 3(b) show the surface of 1 wt. % $\alpha 4T$ in PS, where the protruding structures in Fig. 3(a) and the black circular dots in Fig. 3(b) appear to be mostly $\alpha 4T$ crystallites located near the surface. In

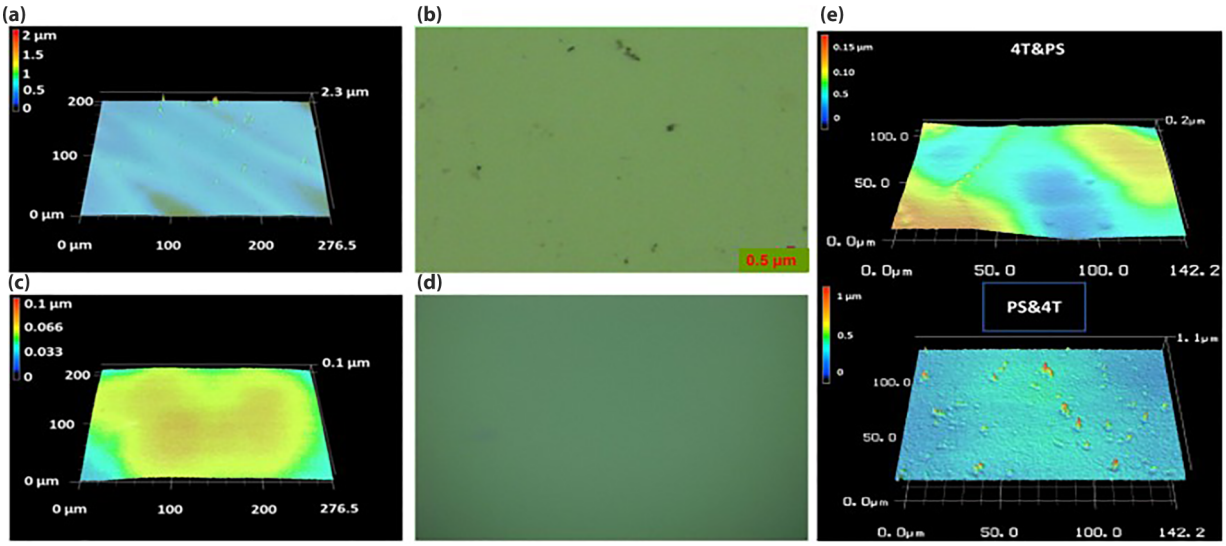

FIG. 3. Three-dimensional laser optical microscopy shows (a) 3D height profile image and (b) laser optical image of the surface of a film with 1 wt. % $\alpha 4T$ in PS at 50 × magnification. Corresponding 3D height (c) and laser optical (d) images are shown for a PS-only film. Scale bar in (b) is 0.5 µm. (e) Comparison of roughnesses of PS bilayers with $\alpha 4T$ in bottom and top layers, showing roughness arising mainly from $\alpha 4T$.

contrast, pure PS films were flat and featureless, with less than 100 nm of surface roughness [Figs. 3(c) and 3(d)]. The surfaces of the PS&PS sample was smoothest with 100 nm or less roughness [Fig. 3(c)], and then $4T$&PS with 200 nm or less roughness [Fig. 3(e)]. This may be because the top layer being PS contributes to a smooth surface. PS&$4T$ samples and $4T$&$4T$ samples had the $4T$ layer on top, which seems to have contributed to surface roughness exceeding 1 um. However, mobilities (discussed in SM Sec. 2.3) were not strongly dependent on this roughness. An additional comparison of $4T$&PS and PS&$4T$ films is shown in Fig. 3(e).

The protruding structures in the films containing $\alpha 4T$ were analyzed via SEM/EDS [Fig. 4(a)]. Figure 4 shows EDS spectra from a 1 wt. % $\alpha 4T$ sample, indicating the presence of $\alpha 4T$ in one of the crystallite-like structures via the presence of the element S [Fig. 4(b)]. Figure 4(c) shows a significantly diminished presence of sulfur in areas without the bright dots, implying the aggregated structures are $\alpha 4T$ crystallites. The substrate used for SEM/EDS was BSG composed of silicon, boron, calcium, magnesium, as well as other alkali oxides for enhancing mechanical properties.

Confocal microscopy of 1 wt. % $\alpha 4T$ in PS samples (Fig. 5) showed localized regions of fluorescence at wavelengths (448-nm excitation and 460–570-nm emission) where $\alpha 4T$ has been shown to fluoresce [30]. PS-only samples showed no such fluorescence, providing further support for the presence of $\alpha 4T$ crystallites for the 1 wt. % $\alpha 4T$ in PS samples.

The sizes are larger than the resolution limit of the experiment, which was < 100 nm.

C. Charge-storage behavior of dielectrics with and without $\alpha 4T$ crystallites

Figure 6 shows an image of a portion of an OFET structure using a laser optical microscope. Charging conditions refer to

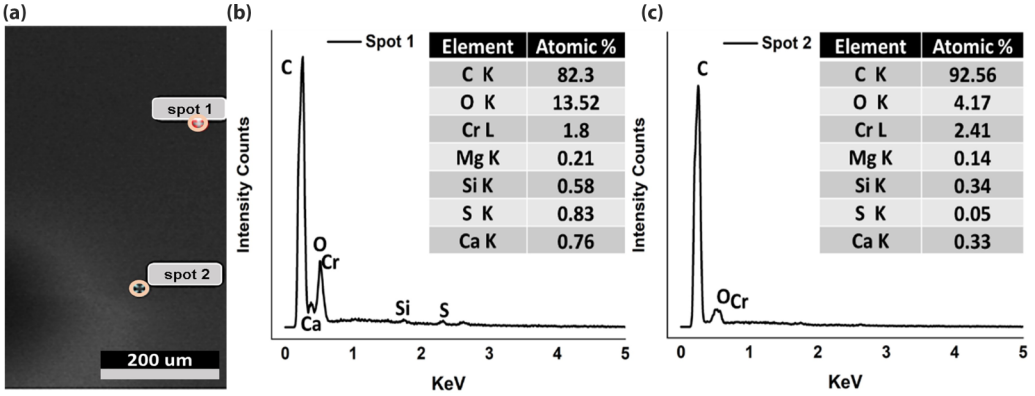

FIG. 4. SEM/EDS of 1 wt. % $\alpha 4T$ in PS dielectric. (a) SEM image of the region scanned and (b) intensity count vs KeV graph of spot 1 with its relative elements and elemental atomic composition, and (c) intensity count vs KeV graph of spot 2 with its relative elements with its relative elements and elemental atomic composition.

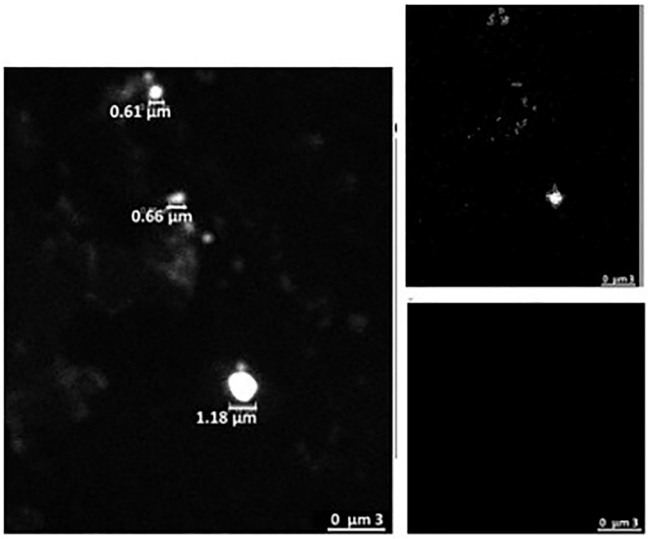

FIG. 5. Confocal microscopy with 448-nm excitation and 460–570-nm emission showing the presence of fluorescing $\alpha 4T$ crystallites. (Left) Length measurements of 0.61-, 0.66-, and 1.18-µm size are indicated. (Right) Additional aggregate structures observed and a film with no $\alpha 4T$ and no emission.

when there is −70 V applied on the top pair of gold source and drain electrodes shown in Fig. 1 while 0 V is applied to the gate of the OFET, while discharging conditions refer to when there is +70 V applied on the source and drain while 0 V is applied to the gate of the OFET.

1. Charge-storage calculations from transfer-curve shifts

Sequences of charging steps were performed on the OFETs to determine charging-induced curve shifts and the retention of those shifts. A charging/discharging sequence refers to

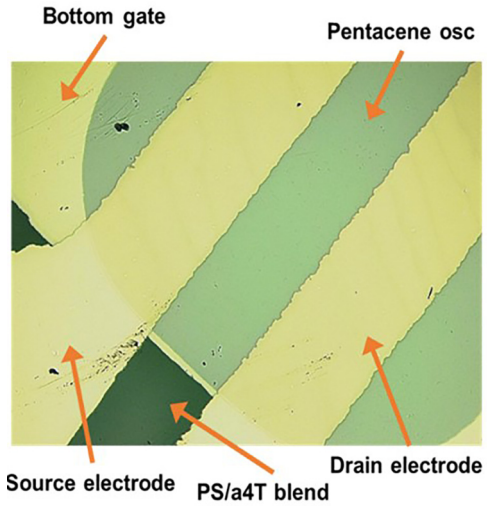

FIG. 6. OFET device structure for transfer/output curve measurements shown as a laser optical microscope image with 20 × magnification. The "bottom gate" is patterned to extend beyond the patterned pentacene. The source and drain cross the entire top of the pentacene. The PS dielectric which may contain $\alpha 4T$ in one or two layers is spin coated over the entire BSG substrate.

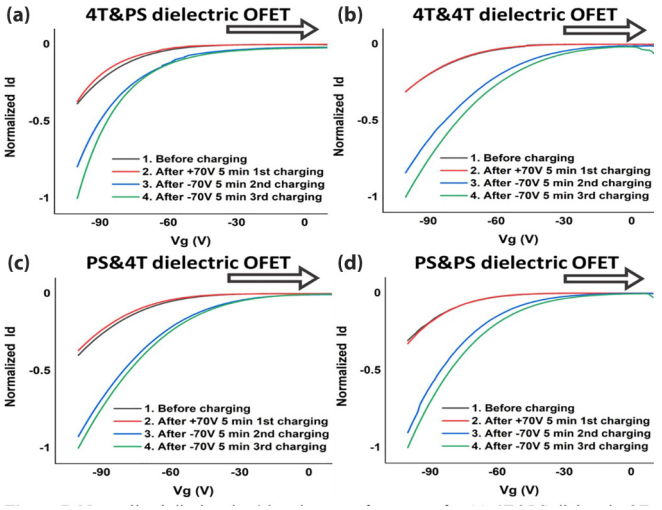

FIG. 7. Normalized discharging/charging transfer curves for (a) $4T$&PS dielectric OFET, (b) $4T$&$4T$ dielectric OFET, (c) PS&$4T$ dielectric OFET, and (d) PS&PS dielectric OFET. Arrows indicate the approximate curve shifts for −70-V charging. All normalization was performed based on the value of I_d at −100 V for each graph.

transfer curves measured before charging, after −70-V/5-min charging, after +70-V/5-min discharging, and after another +70-V/5-min discharging. Discharging/charging refers to transfer curves measured before charging, after +70-V/5-min discharging, after −70-V/5 min charging, and after another −70-V/5-min charging. Figures 7 and 8 show the general perturbations resulting from these charging and discharging procedures in the form of average normalized transfer curves. This allows multiple observations of each device configuration to contribute to the displayed trends.

As shown in Fig. 7, for each of the four types of OFETs, in a discharging/charging sequence, the initial +70 V/5-min dis-

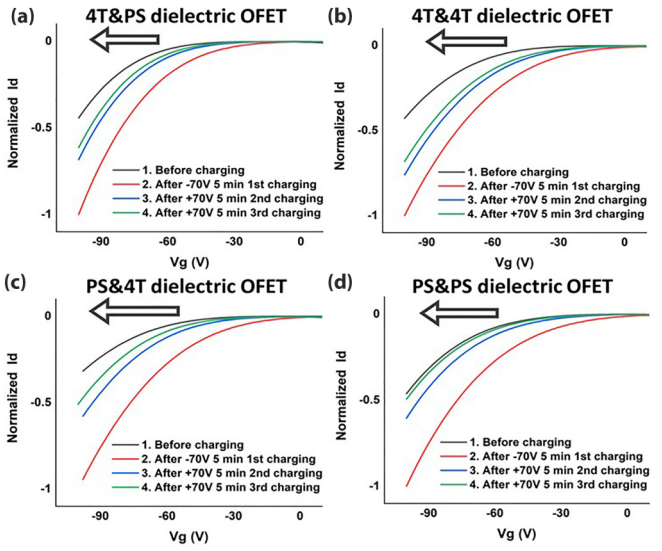

FIG. 8. Normalized charging/discharging transfer curves for (a) $4T$&PS dielectric OFET, (b) $4T$&$4T$ dielectric OFET, (c) PS&$4T$ dielectric OFET, and (d) PS&PS dielectric OFET. Arrows indicate the approximate curve shifts for +70-V discharging.

TABLE I. (a) Averaged value of number of charges stored/released for each of the transfer curves of the discharging/charging cycle to calculate total charges stored for all four types of samples. The total charges stored (3 + column 4–column 2) divided by total volume of each sample (refer to Sec. 2.5 of SM). (b) Averaged value of number of charges stored/released for each of the transfer curves of the charging/discharging cycle to calculate charge retention for all four types of samples. The stored charge retention is (column 2–column 3–column 4)/column 2.

(a)

Charges stored/released *Positive – released *Negative – stored	after 1 70V 5 min ID	after 2 -70V 5 min ID	after 3 -70V 5 min ID	Volume charge density (charges / cm^3)
Ave. PS&PS	$3.0x10^8 \pm 5.5x10^7$	$-1.3x10^9 \pm 5.2x10^8$	$-1.1x10^9 \pm 7.6x10^8$	$7.0x10^{15} \pm 4.3x10^{15}$
Ave. PS&4T	$9.4x10^7 \pm 6.4x10^7$	$-3.0x10^9 \pm 6.2x10^8$	$-1.1x10^9 \pm 6.2x10^8$	$1.3x10^{16} \pm 4.5x10^{15}$
Ave. 4T&PS	$1.5x10^8 \pm 1.3x10^8$	$-2.8x10^9 \pm 1.1x10^9$	$-8.9x10^8 \pm 4.6x10^8$	$1.2x10^{16} \pm 5.7x10^{15}$
Ave. 4T&4T	$9.9x10^6 \pm 2.4x10^8$	$-2.8x10^9 \pm 1.5x10^9$	$-6.2x10^9 \pm 1.7x10^8$	$1.2x10^{16} \pm 6.4x10^{15}$

(b)

Charges stored/released *Positive – released *Negative – stored	after 1 -70V 5 min ID	after 2 70V 5 min ID	after 3 70V 5 min ID	Stored Charge Retention (%)
Ave. PS&PS	$-2.0x10^9 \pm 3.9x10^8$	$1.1x10^9 \pm 1.6x10^8$	$5.9x10^8 \pm 4.0x10^8$	16 %
Ave. PS&4T	$-3.1x10^9 \pm 4.4x10^8$	$1.6x10^9 \pm 1.9x10^8$	$5.3x10^8 \pm 2.4x10^8$	31 %
Ave. 4T&PS	$-3.9x10^9 \pm 1.3x10^9$	$1.6x10^9 \pm 1.4x10^9$	$4.4x10^8 \pm 2.9x10^8$	48 %
Ave. 4T&4T	$-3.8x10^9 \pm 8.5x10^8$	$9.8x10^8 \pm 1.2x10^8$	$7.4x10^8 \pm 5.7x10^8$	55 %

charging causes minimal change in the OFET transfer curve, and then the subsequent −70-V/5-min charging steps induce progressive shifts of the transfer curve to lower magnitude of the gate voltage (V_{GS}), corresponding to increased drain current (I_d) at a given V_{GS}. In contrast, in the charging/discharging sequences, the initial −70-V/5-min charging induces a large shift of the transfer curve to lower V_{GS} magnitude, and then the +70-V/5-min discharging steps cause sequential shifts back to larger-magnitude V_{GS} (Fig. 8).

These curve shifts are associated with changes in V_{TH}, which are typically calculated as extrapolations to $I_D = 0$ of $\sqrt{|I_D|}$ vs V_{GS} graphs. The data presented in Figs. 7 and 8 are replotted as $\sqrt{|I_D|}$ vs V_{GS} graphs in Fig. S3 and Fig. S4, respectively [31]. The curvatures of these graphs make the necessary extrapolations imprecise. Therefore, derivatives of the individual $\sqrt{|I_D|}$ vs V_{GS} graphs from these experiments were taken with respect to V_{GS} to obtain plots of $\sqrt{|I_D|}'$ and then $\sqrt{|I_D|}''$ vs V_{GS}. These latter plots were used to calculate values of "a" (the maxima in the $\sqrt{|I_D|}''$ vs V_{GS} curves) whose shifts correspond to shifts in V_{TH} of each curve from procedures outlined in Sec. 2.3 of the SM as shown in Figs. S5–S8. Subsequently, Δa applied to Eq. (S4) gave the total number of charges stored/released for each charging sequence. The same procedure was repeated for at least three samples per type of bilayer sample for each of the charging cycles. Average charges stored/released for each of the four sample types are shown in Table I for charging/discharging cycles [Table I(a)], and discharging/charging cycles [Table I(b)]. All three samples incorporating $\alpha 4T$ captured more charge from the "charging" process than did the one without $\alpha 4T$. It seems that the limit of charge incorporation for the field applied was reached with less than half of the crystallites that would be in a $4T\&4T$ bilayer charged. The fact that increased charge storage occurred regardless of whether the $\alpha 4T$ was at the pentacene interface suggests that this is a bulk charge-storage effect rather than interfacial polarization or Maxwell-Wagner effects. Note that the increase in stored charge from the presence of $\alpha 4T$ should not arise significantly from any increased relative permittivity of $\alpha 4T$; its solid-state relative permittivity is about 3.5 [21], only slightly higher than that of polystyrene, and it is present at a minimal volume fraction.

Charging/discharging cycles showed that PS&PS samples had the smallest degree of stored charge retention after the full charging/discharging cycle at around 16%; $4T\&4T$ had the highest charge retention at around 55%, then $4T\&$PS at around 46%, and PS&$4T$ at around 29%. This suggests that charges stored in the dielectrics localize around the $\alpha 4T$ crystallites. KPFM measurements further validated this theory in the upcoming Sec. III C 2. Charges appear to be stored in a more stable state when stored in $4T\&$PS compared to PS&$4T$, with the charge-localizing $\alpha 4T$ crystallites further from the pentacene OSC in which charges may be recombined.

Discharging/charging cycles showed that PS&PS had the lowest number density of charges stored, while all other samples containing $\alpha 4T$ crystallites had similar number of charges stored under the conditions of these experiments. We postulate that this was because the maximum charge-storage capacity was not reached yet for the other three types of samples. Experiments on maximum charge-storage capacity are discussed in Sec. III C 3.

2. Localized charge storage around α4T via KPFM

Crystallite locations and dimensions as visualized by protrusions at the PS surface were first identified from Atomic

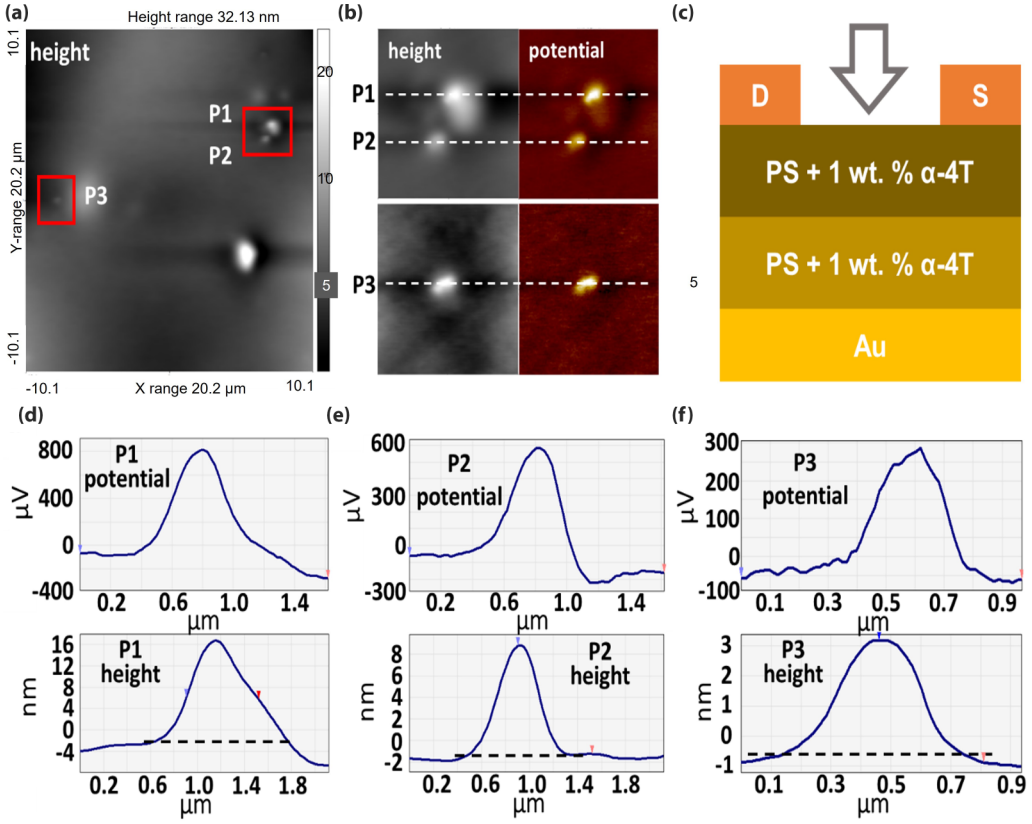

FIG. 9. KPFM of 4*T*&4*T* bilayer sample before charging. (a) Height-profile measurement using KPFM of 20.2−µm × 20.2−µm area with three observed crystallites P1, P2, and P3. (b) Height and electric potential measurement by KPFM over region identified for P1, P2, and P3. (c) Schematic of device structure identifying region of sample scanned via KPFM. (d) Potential and height measurements across line P1 in (b) containing P1 crystallite. (e) Potential and height measurements across line P2 in (b) containing P2 crystallite. (f) Potential and height measurements across line P3 in (b) containing P3 crystallite.

Force Microscopy (AFM) height-profile scans as shown in Figs. 9(a) and 10(a). Height and electrical potential scans were subsequently performed on the identified regions as shown in Figs. 9(b) and 10(b). The device used for charging is shown in Fig. S12. All scans were performed between the top electrodes on the 4*T*&4*T* samples before charging and after charging as outlined in Fig. 9(c). Seven crystallites' (identified as P1–P7) height and electric potential were measured before charging as shown in Figs. 9(d)–9(f) and Figs. 10(c)–10(f). The seven identified crystallites (P1–P7) before charging had an average of 370-µV maximum electrical potential difference, average maximum protrusion of 9 nm, and average width of 1.1 µm. KPFM scans were also performed after charging for four crystallites, whose height and electric potential measurements are shown in Fig. 11. The four crystallites measured by KPFM after charging (Fig. 11) had an average of 1300-µV maximum electrical potential difference, average maximum height of 7.8 nm, and average width of 0.75 µm. The measured average width of the crystallites is in good agreement with measurements from confocal microscopy (Fig. 5). It is, however, possible that the protrusions included were conformal coatings of PS over crystallites embedded at a finite depth from the top surface.

We assume that the amount of charge stored in a crystallite is proportional to the capacitance between the tip and the PS *around* the crystallite, and the voltage measured over the crystallite. This only requires that the reference (silver paste) electrode equilibrate zero voltage to the gold electrodes, and thus to the polymer film in general (Fig. S12), with the crystallites being perturbations of that reference voltage. We have measured the difference in film capacitance before and after charging and found it to be insignificant for samples with < 2 wt. % of crystallites, where there is no percolation among crystallites.

The average tip-to-sample potential differences at the crystallites relative to the surroundings for before charging [Table SIII(a), P1–P7] and after charging [Table SIII(b), P1A–P4A] were calculated to be 370 and 1300 µV, respectively. This suggests that there is $\sim 3.5\times$ higher concentration of charges stored near the crystallites after charging compared to before charging, supporting the conclusion from Sec. III B 2 that charges are localized near the crystallites in PS dielectrics when they are charged in the polarity that favors charge injection.

3. Maximum charge-storage capacity of 4T&PS, 4T&4T, PS&4T, *and PS&PS before dielectric discharge or loss of dielectric stability*

Once the maximum charge-storage capacity of the dielectrics in OFETs is reached during charging, subsequent charging results in breakdown, with a net decrease in transfer-

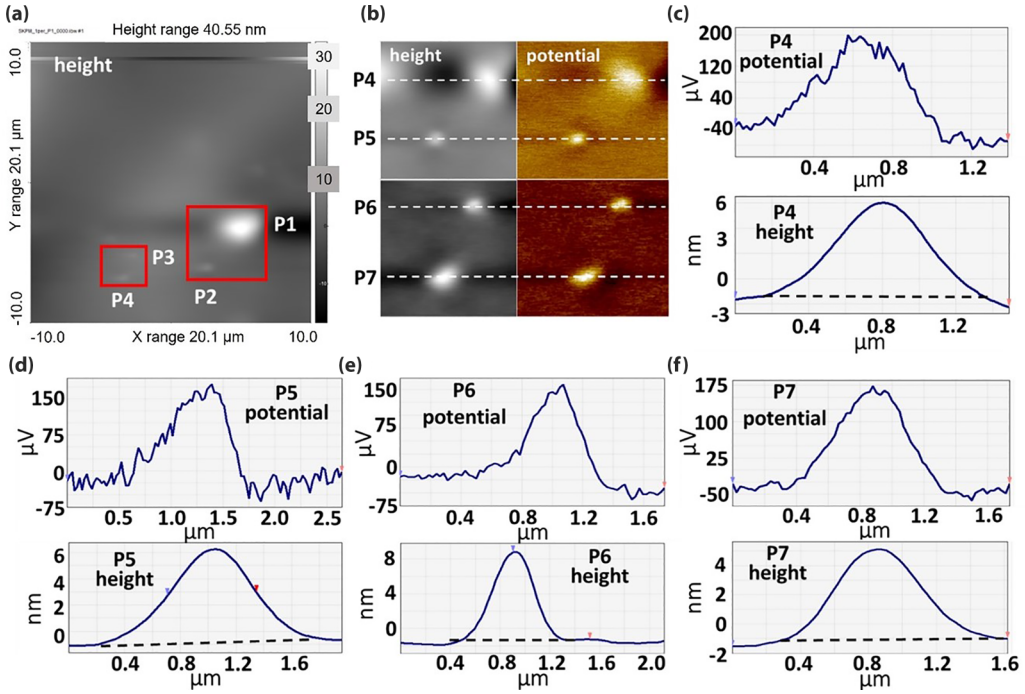

FIG. 10. KPFM of $4T\&4T$ bilayer sample before charging. (a) Height-profile measurement using KPFM of 20.2−µm × 20.2−µm area with four observed crystallites: P4, P5, P6, and P7. (b) Height and electric potential measurement by KPFM over region identified for P4, P5, P6, and P7. (c) Potential and height measurements across line P4 in (b) containing P4 crystallite. (d) Potential and height measurements across line P5 in (b) containing P5 crystallite. (e) Potential and height measurements across line P6 in (b) containing P6 crystallite. (f) Potential and height measurements across line P7 in (b) containing P7 crystallite.

curve current values from subsequent −70-V charging cycles (Fig. 12). This also serves as a test of operational endurance. Maximum charge-storage capacity evaluations were made where OFETs were charged systematically until either (i) a decrease in drain current at $V_{GS} = -70$ V compared to transfer curves before charging, or (ii) a burst release of charges

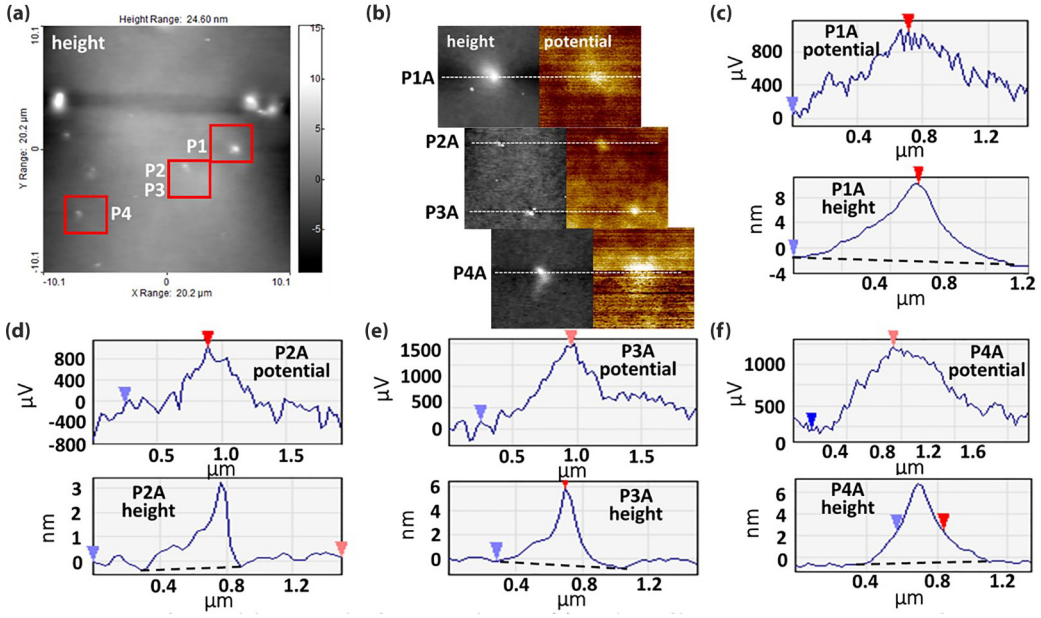

FIG. 11. KPFM of $4T\&4T$ bilayer sample after 5-min charging. (a) Height-profile measurement using KPFM of 20.2−µm × 20.2−µm area with four observed crystallites: P1A, P2A, P3A, and P4A. (b) Height and electric potential measurement by KPFM over region identified for P1A, P2A, P3A, and P4A. (c) Potential and height measurements across line P1A in (b) containing P1A crystallite. (d) Potential and height measurements across line P2A in (b) containing P2A crystallite. (e) Potential and height measurements across line P3A in (b) containing P3A crystallite. (f) Potential and height measurements across line P4A in (b) containing P4A crystallite.

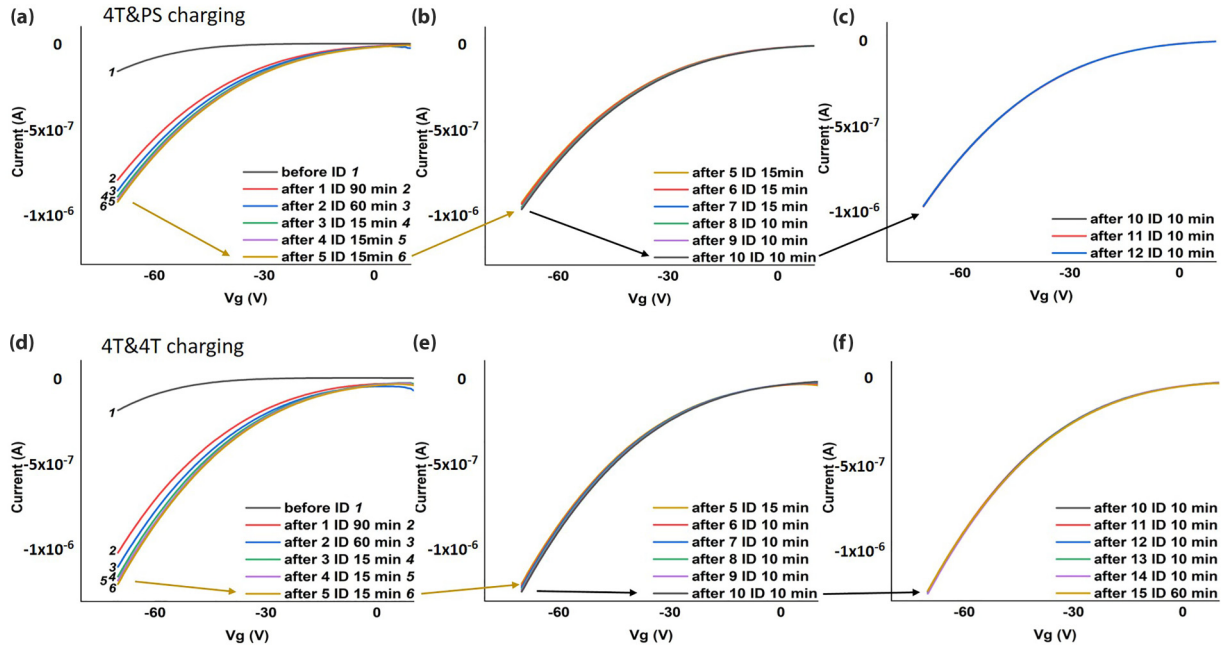

FIG. 12. Charging to maximum capacity transfer curves after charging cycles. (a) Transfer curves before and after five charging cycles for 4*T*&PS sample. (b) Transfer curves after 5–10 charging cycles for 4*T*&PS sample. (c) Transfer curves after 10–12 charging cycles for 4*T*&PS sample. Decrease in I_D at $V_{GS} = -70$ V was observed for transfer curve after 12 ID, showing charge-storage saturation of the 4*T*&PS sample. (d) Transfer curves before and after five charging cycles for 4*T*&4*T* sample. (e) Transfer curves after 5–10 charging cycles for 4*T*&4*T* sample. (f) Transfer curves after 10–15 charging cycles for 4*T*&4*T* sample. Decrease in I_D at -70 V_{GS} was observed for the transfer curve after the 15th charging cycle, showing charge-storage saturation of the 4*T*&4*T* sample. "Before ID 1" means ID plotted before the first charging. "After x" means charging after curve *x* was recorded.

leading to destabilization of the dielectric was observed. (These two criteria are similar to criteria established for dielectric breakdown voltages.) [32–34] For testing efficiency, the first two charging cycles were 90 and 60 min, with ensuing charging cycles of 10-min duration. OFET samples 4*T*&PS and PS&4*T* exhibited slow release of excess charges without burst release of charges. Decrease in drain current at $V_{GS} = -70$ V after charging was used as the criterion for maximum charge storage to have been reached for those samples. These samples were thus stable to at least 5 total hours of charging time (in air), which would be much more demanding than ordinary operational time. OFET samples 4*T*&4*T* and PS&PS additionally exhibited burst release of charges, as another indication of charge-storage saturation for those dielectrics.

Charging to maximum capacity is shown in Figs. 12(a)–12(c) for 4*T*&PS and Figs. 12(d)–12(f) for 4*T*&4*T*. Maximum charging capacity was observed from decrease in drain current at $V_{GS} = -70$ V for both 4*T*&PS and 4*T*&4*T* transfer curves. Figure S13 shows specifically at 2178 s (321.3 min) out of 3600 s during the 15th charging cycle, maximum charging capacity of the 4*T*&4*T* samples was reached as evident from the burst release of charges at this time, which we assume was a sign of breakdown of the charge-storing system. Sometimes a brief flash of light was observed at the time of this burst of charges. Charging to maximum capacity is shown in Figs. 13(a)–13(c) for PS&4*T* and Fig. 13(d) for PS&PS. Maximum charging capacity was observed as a decrease in transfer-curve current between curves 5 and 6 for PS&4*T*, while transfer-curve destabilization was observed in PS&PS during acquisition of curve 4.

Two parameters, maximum charges stored as determined by Δa, and charging time to maximum capacity (a measure of durability as well as charge-storage capacity) were analyzed from Sec. II B 3 was used to derive parameter *a* for transfer curves in Figs. 12 and 13. Subsequently, the product of dielectric capacitance and Δa was used to calculate maximum cumulative charges stored, shown in Table II. Similar results were observed for both parameters for 4*T*&PS and PS&4*T* samples, showing that the $\alpha 4T$ crystallite content is the critical factor controlling the maximum volume-charge density (VCD) of dielectrics. Table II shows that compared to PS&PS, PS&4*T* as well as 4*T*&PS had 46% increased maximum VCD while 4*T*&4*T* had 69% more maximum VCD. The percentage of maximum VCD reached after 5-min charging (Table III) was calculated by comparing the maximum VCD (from Table II) to volume-charge density after 50-min/−70-V charging (from Table I). PS&PS reached 75% of maximum VCD after 5-min charging whereas samples containing 4*T* reached an average 91% of maximum VCD after 5-min charging.

4. Dielectric breakdown experiments to investigate charge movement under electrical bias

The free-volume theory of dielectric breakdown postulates that dielectric breakdown of polymers in high electric field occurs by electrons accelerating in free volume in polymer dielectrics at high electric fields [13]. It has been proposed that for polystyrene specifically, strong electric fields induce pi-pi reorganization perpendicular to the electric field, forming a path in which charge carriers can accelerate to cause

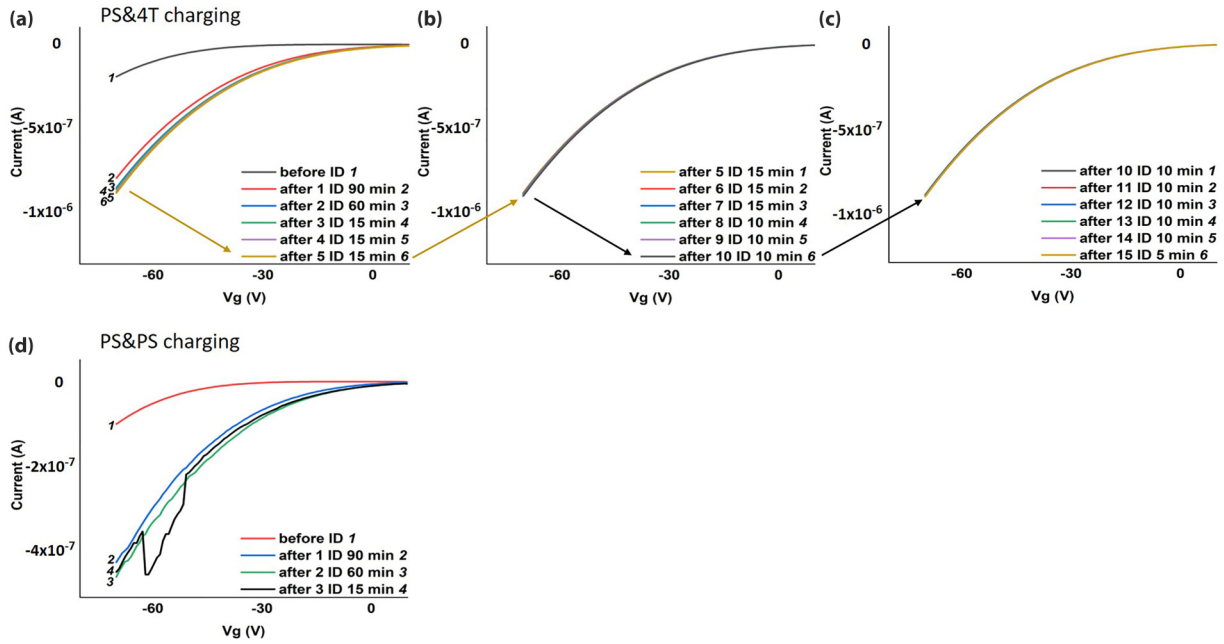

FIG. 13. Charging to maximum capacity transfer curves after charging cycles. (a) Transfer curves before and after five charging cycles for PS&4T sample. (b) Transfer curves after 5–10 charging cycles for PS&4T sample. (c) Transfer curves after 10–15 charging cycles for PS&4T sample. Decrease in I_D at $V_{GS} = -70$ V was observed for transfer curve after 15 "ID" showing saturation of dielectric of PS&4T sample. (d) Transfer curves before and after three charging cycles for PS&PS sample. Destabilization of transfer curve after 3 ID indicates saturation of dielectric of PS&PS sample.

an avalanche of electrons, breaking down the polystyrene dielectric [14].

Based on this, we performed dielectric breakdown experiments on the four dielectric configurations in capacitor structures (Fig. 14). Even at 300-V net electrical bias, 4T&PS did not show notable dielectric breakdown, which was a clearly discernible improvement over the other bilayers. Further details are given in the Supplemental Material.

IV. DISCUSSION AND CONCLUSION

Positive charging at the source and drain electrodes (discharging) can result in electrons in the dielectric being drawn into the pentacene OSC as shown in Fig. 15(a). This would lead to hole trapping in the pentacene OSC by those electrons, decreasing the conductance, a form of bias stress. This increases V_{TH}, because more gate voltage needs to be applied to fill the traps. On the other hand, negative charging at the

TABLE II. Derived parameter "a" values for calculating maximum charges stored for each of the four types of samples and the charge times to maximum capacity. The thickness of PS&PS was 5501 nm, PS&4T was 5205 nm, 4T&PS was 5061 nm, and 4T&4T was 5113 nm.

Samples	Before ID "a"	After 2 ID "a"	Max. Charges Stored	Charge Time to Max. Capacity	Max. Volume Charge Density (charges/cm^3)
PS&PS	10	-22	2.7x10^9	Less than 150 min	*8.9 x 10^{15} charges/cm^3*
	Before ID "a"	After 14 ID "a"	Max. Charges Stored	Charge Time to Max. Capacity	Max. Volume Charge Density (charges/cm^3)
PS&4T	6.0	-32	3.6x10^9	285 min	*1.3 x 10^{16} charges/cm^3*
	Before ID "a"	After 11 ID "a"	Max. Charges Stored	Charge Time to Max. Capacity	Max. Volume Charge Density (charges/cm^3)
4T&PS	3.6	-38	3.7x10^9	265 min	*1.3 x 10^{16} charges/cm^3*
	Before ID "a"	After 14 ID "a"	Max. Charges Stored	Charge Time to Max. Capacity	Max. Volume Charge Density (charges/cm^3)
4T&4T	9.8	-41	4.3x10^9	321.3 min	*1.5 x 10^{16} charges/cm^3*

TABLE III. Percentage of maximum VCD reached after 5-min charging was calculated by comparing the maximum VCD from Table II to volume charge density after −70-V/5-min charging from Table I.

	Ave. Volume Charge Density (charges/cm^3) after -70V 5min (Table 1b.)	Max. Volume Charge Density (charges/cm^3) from Table 2	% of Max. Volume Charge Density reached after 5 min charging
PS&PS	$6.7x10^{15} \pm 1.6x10^{8}$	8.9×10^{15}	75 %
PS&4T	$1.1x10^{9} \pm 1.9x10^{8}$	1.3×10^{16}	85 %
4T&PS	$1.3x10^{9} \pm 1.4x10^{9}$	1.3×10^{16}	100 %
4T&4T	$1.3x10^{8} \pm 1.2x10^{8}$	1.5×10^{16}	87 %

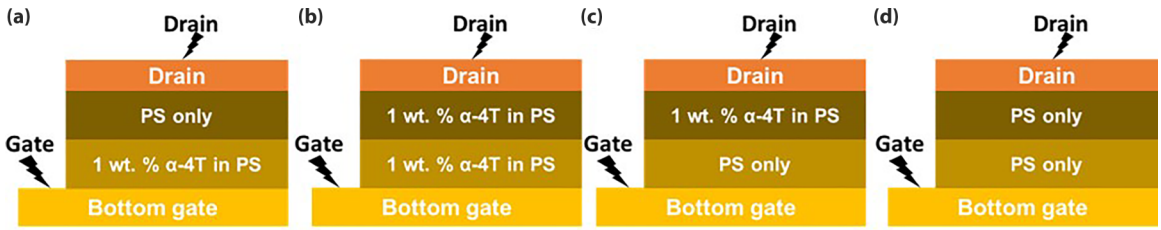

FIG. 14. Device structure for dielectric breakdown experiments of (a) 4*T*&PS, (b) 4*T*&4*T*, (c) PS&4*T*, and (d) PS&PS.

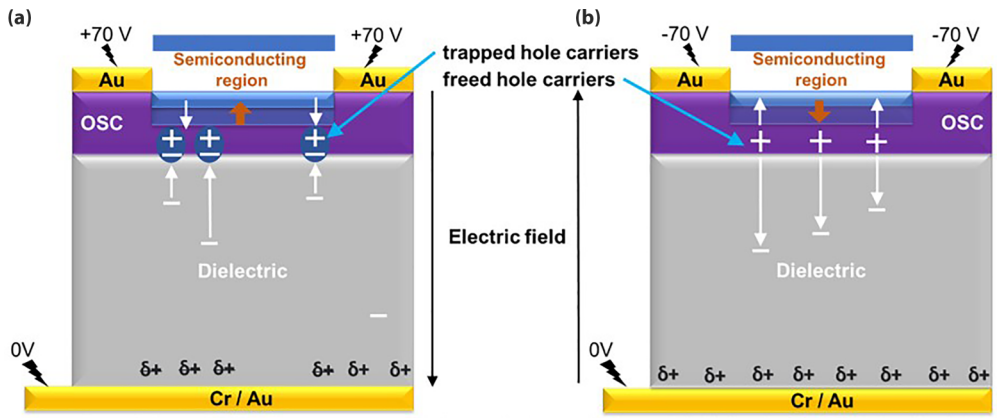

FIG. 15. (a) Schematic showing movement of charges in OFET devices with dielectric made of PS-only during positive charging. (b) Movement of charges in the same device with negative charging.

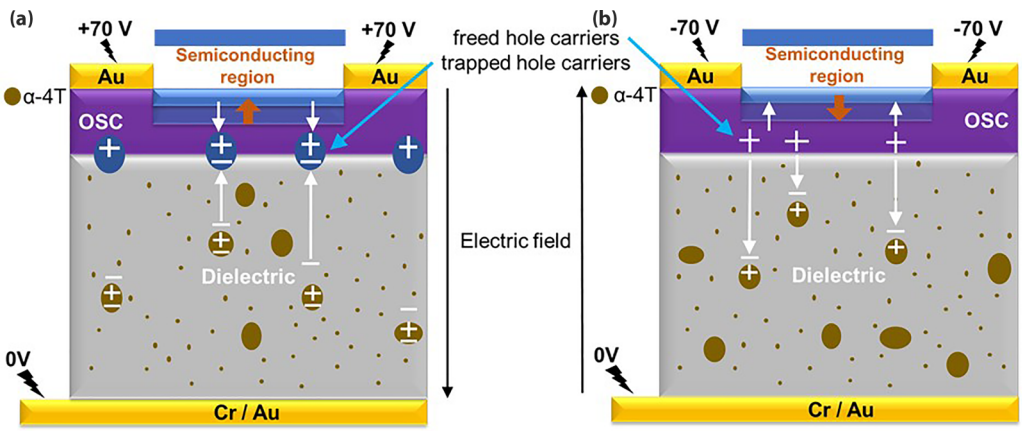

FIG. 16. (a) Schematic showing movement of charges in OFET devices with dielectric made of PS with $\alpha 4T$ crystallites during positive charging. Electron injection into the pentacene from the dielectric is inhibited by the electrons being attracted to positively charged crystallites. (b) Schematic showing movement of charges in the same devices during negative charging. Electron injection from pentacene into the dielectric is promoted, increasing the concentration of mobile holes in the pentacene.

source-drain electrodes leads to creation of holes in the pentacene left behind by electrons injected into the dielectric, as shown in Fig. 15(b), increasing the conductance. This decreases V_{TH}, because these created holes can fill traps, so less gate voltage is needed before mobile holes are induced. Another way to view this V_{TH} decrease is as an additional electric field imposed in series with the applied gate field, with the positive voltage near the gate electrode and the negative voltage in the dielectric, again as shown in Fig. 15(b).

OFETs with $\alpha 4T$ in PS show analogous but in many cases differentiated charging responses. Positive charging gave less bias stress with $\alpha 4T$ present, possibly because electrons were held more tightly by positive charges localized on crystallites, inhibiting their injection into pentacene, as shown schematically in Fig. 16(a). Negative charging gave larger current increases as electrons were injected more readily into the dielectric, where they would be partially compensated by positively charged crystallites, and also stabilize holes left behind in the pentacene possibly because of a higher electric field in series with the gate, as shown schematically in Fig. 16(b).

The behavior of charges in and around electroactive $\alpha 4T$ crystallites in dielectric PS matrix at varying positions was investigated. XRD, SEM/EDS, and confocal microscopy proved the formation of $\alpha 4T$ crystallites in the PS matrix. A modified saturation-regime current-voltage relationship was used to derive parameter a, a marker of shifting V_{TH}, to calculate Δa for OFET transfer curves before and after charging. Charges stored/released upon charging of OFET devices were quantified by the Δa and capacitance measurements. Results showed that $\alpha 4T$ crystallites increased maximum charge-storage capacity as well as charge-retention capability of dielectrics. KPFM experiments showed that charges localize near the $\alpha 4T$ crystallites upon charging, validating the point that $\alpha 4T$ crystallites in PS affect the electrical properties of the dielectric and therefore OFET devices. Trilayer experiments (Sec. 3.3.4 of SM) validated the charge-retention improvement of $\alpha 4T$ crystallite embedded PS dielectrics. It was also noted that better charge retention was observed for $4T$&PS dielectric OFETs compared to PS&$4T$ dielectric OFETs. This was attributed to $4T$&PS storing of injected electrons farther from the source of potential bias. Similar phenomena were observed in dielectric breakdown experiments (Sec. 3.3.5 of SM) of $4T$&PS to prevent dielectric breakdown, highlighting the importance of the location of electroactive crystallites on the electrical properties of engineered electrical devices. These bulk effects are more likely contributors to charge storage than the minimal interfacial polarization expected from a pentacene-PS interface [35]. The observed charge-storage behavior of electroactive crystallite embedded dielectric layers may be harnessed to enhance dielectrics used for capacitive energy storage [36,37].

ACKNOWLEDGMENT

This work was supported by the US Department of Energy, Office of Science, Basic Energy Sciences, Materials Chemistry Program, under Award No. DE-FG02-07ER46465.

[1] J. Mei, Y. Diao, A. L. Appleton, L. Fang, and Z. Bao, Integrated materials design of organic semiconductors for field-effect transistors, J. Am. Chem. Soc. **135**, 6724 (2013).

[2] C. Wang, H. Dong, W. Hu, Y. Liu, and D. Zhu, Semiconducting π-conjugated systems in field-effect transistors: A material odyssey of organic electronics, Chem. Rev. **112**, 2208 (2012).

[3] C. Zhang, P. Chen, and W. Hu, Organic field-effect transistor-based gas sensors, Chem. Soc. Rev. **44**, 2087 (2015).

[4] Y. Guo, G. Yu, and Y. Liu, Functional organic field-effect transistors, Adv. Mater. **22**, 4427 (2010).

[5] H. Sirringhaus, Device physics of solution-processed organic field-effect transistors, Adv. Mater. **17**, 2411 (2005).

[6] H. Sirringhaus, 25th anniversary article: Organic field-effect transistors: The path beyond amorphous silicon, Adv. Mater. **26**, 1319 (2014).

[7] G. Horowitz, R. Hajlaoui, H. Bouchriha, R. Bourguiga, and M. Hajlaoui, The concept of "threshold voltage" in organic field effect transistors, Adv. Mater. **10**, 923 (1999).

[8] H. Li, W. Shi, J. Song, H.-J. Jang, J. Dailey, J. Yu, and H. E. Katz, Chemical and biomolecule sensing with organic field-effect transistors, Chem. Rev. **119**, 3 (2019).

[9] A. A. Virkar, S. Mannsfeld, Z. Bao, and N. Stingelin, Organic semiconductor growth and morphology considerations for organic thin-film transistors, Adv. Mater. **22**, 3857 (2010).

[10] J. Li, Y. Zhao, H. S. Tan, Y. L. Guo, C. A. Di, G. Yu, Y. Q. Liu, M. Lin, S. H. Lim, Y. H. Zhou, H. B. Su, and B. S. Ong, A stable solution-processed polymer semiconductor with record high-mobility for printed transistors, Sci. Rep. **2**, 754 (2012).

[11] C. Berggren, B. Bjarnason, and G. Johansson, Capacitive biosensors, Electroanalysis **13**, 173 (2001).

[12] C. Huang and Q. Zhang, Enhanced dielectric and electromechanical responses in high dielectric constant all-polymer percolative composites, Adv. Funct. Mater. **14**, 501 (2004).

[13] Y. Wang, X. Zhou, Q. Chen, B. Chu, and Q. Zhang, Recent development of high energy density polymers for dielectric capacitors, IEEE Trans. Dielectr. Electr. Insu. **17**, 1036 (2010).

[14] P. Hu, Y. Shen, Y. Guan, X. Zhang, Y. Lin, Q. Zhang, and C.-W. Nan, Topological-structure modulated polymer nanocomposites exhibiting highly enhanced dielectric strength and energy density, Adv. Funct. Mater. **24**, 3172 (2014).

[15] Q. Zhang, B. Barrett, T. Lee, T. Mukhopadhyaya, C. Lu, E. C. Plunkett, T. Kale, C. Chi, K. J. T. Livi, P. McGuiggan, D. H. Reich, S. Thon, A. E. Bragg, and H. E. Katz, Maximized hole trapping in a polystyrene transistor dielectric from a highly branched iminobis(aminoarene) side chain, ACS Appl. Mater. Interfaces **13**, 34584 (2021).

[16] O. J. Alley, E. Plunkett, T. S. Kale, X. Guo, G. McClintock, M. Bhupathiraju, B. J. Kirby, D. H. Reich, and H. E. Katz, Synthesis, fabrication, and heterostructure of charged, substituted polystyrene multilayer dielectrics and their effects in pentacene transistors, Macromolecules **49**, 3478 (2016).

[17] Q. Zhang, T. S. Kale, E. Plunkett, W. Shi, B. J. Kirby, D. H. Reich, and H. E. Katz, Highly contrasting static charging and bias stress effects in pentacene transistors with polystyrene heterostructures incorporating oxidizable N,N′-Bis(4-methoxyphenyl)aniline side chains as gate dielectrics, Macromolecules **51**, 6011 (2018).

[18] E. C. Plunkett, Q. Zhang, H. E. Katz, and D. H. Reich, Charge trapping in polymer electrets with highly dilute blended aryl-amine donors, ACS Appl. Electron. Mater. **3**, 1656 (2021).

[19] E. Plunkett, T. S. Kale, Q. Zhang, H. E. Katz, and D. H. Reich, Effects of trifluoromethyl substituents on interfacial and bulk polarization of polystyrene gate dielectrics, Appl. Phys. Lett. **114**, 023301 (2019).

[20] M. A. Reijme, M. W. G. Ponjée, A. W. Denier van der Gon, and H. H. Brongersma, Molecular orientation and morphology of contact printed α-quaterthiophene films on gold, Appl. Surf. Sci. **200**, 27 (2002).

[21] A. Sassella, D. Braga, M. Campione, T. Ciabattoni, M. Moret1, J. Parravicini, and G. B. Parravicini, Probing phase transitions and stability of organic semiconductor single crystals by dielectric investigation, J. Appl. Phys. **109**, 013529 (2011).

[22] H. Koezuka, A. Tsumura, and T. Ando, Field-effect transistor with polythiophene thin film, Synth. Met. **18**, 699 (1987).

[23] D. Y. W. Ng, R. Vill., Y. Wu, K. Koynov, Y. Tokura, W. Liu, S. Sihler, A. Kreyes, S. Ritz, H. Barth, U. Ziener, and T. Weil, Directing intracellular supramolecular assembly with N-heteroaromatic quaterthiophene analogues, Nat. Commun. **8**, 1850 (2017).

[24] R. D. McCullough, The chemistry of conducting polythiophenes, Adv. Mater. **10**, 93 (1998).

[25] Y. Zhao and D. G. Truhlar, Design of density functionals that are broadly accurate for thermochemistry, thermochemical kinetics, and nonbonded interactions, J. Phys. Chem. A **109**, 5656 (2005).

[26] L. Goerigk, A. Hansen, C. Bauer, S. Ehrlich, A. Najibi, and S. Grimme, A look at the density functional theory zoo with the advanced GMTKN55 database for general main group thermochemistry, kinetics and noncovalent interactions, Phys. Chem. Chem. Phys. **19**, 32184 (2017).

[27] F. Neese, The ORCA program system, Wiley Interdiscip. Rev. Comput. Mol. Sci. **2**, 73 (2012).

[28] V. Barone and M. Cossi, Quantum calculation of molecular energies and energy gradients in solution by a conductor solvent model, J. Phys. Chem. A **102**, 1995 (1998).

[29] K. J. Thorley, T. W. Finn, K. Jarolimek, J. E. Anthony, and C. Risko, Theory-driven insight into the crystal packing of Trialkylsilylethynyl Pentacenes, Chem. Mater. **29**, 2502 (2017).

[30] S. Ghosh, B. Jana, A. Ghosh, D. M. Guldi, and A. Patra, The impact of aggregation of quaterthiophenes on the excited state dynamics, J. Phys. Chem. Lett. **12**, 3424 (2021).

[31] See Supplemental Material at http://link.aps.org/supplemental/10.1103/PhysRevMaterials.7.065003 for details about film and device fabrication methods [16,17,22,38–41]; film and device characterization [30,42]; film characterization and measurements; mobility and parameter *a* calculations; calculations for number of charges stored; *V*TH calculation [7,43,44]; *IV* curve showing burst release of $4T\&4T$ sample during charging; charge-storage calculation, charge retention, and dielectric breakdown experiments [45,46]; and representative individual transfer curves of OFET devices, which includes Refs. [7,16,17,22,30].

[32] A. Andersen and J. R. Dennison, In an enhanced operational definition of dielectric breakdown for DC voltage step-up tests, in *Proceedings of the IEEE CEIDP* (IEEE, Piscataway, NJ, 2017), p. 433.

[33] M. Kathaperumal, Y. Kim, L. R. Johnstone, J. P. Tillotson, Y. Park, M. J. Pan, and J. W. Perry, Enhanced energy density and extraction efficiency of polar sol-gel dielectric films with reduced residual ions, J. Mater. Chem. C **8**, 17395 (2020).

[34] Y. Kim, M. Kathaperumal, V. W. Chen, Y. Park, C. Fuentes-Hernandez, M. J. Pan, B. Kippelen, and J. W. Perry, Bilayer structure with ultrahigh energy/power density using hybrid sol-gel dielectric and charge-blocking monolayer, Adv. Energy Mater. **5**, 1500767 (2015).

[35] Y. Wu, G. Haugstad, and C. D. Frisbie, Electronic polarization at pentacene/polymer dielectric interfaces: Imaging surface potentials and contact potential differences as a function of substrate type, growth temperature, and pentacene microstructure, J. Phys. Chem. C **118**, 2487 (2014).

[36] S. Lee, J. Hong, and K. Kang, Redox-active organic compounds for future sustainable energy storage system, Adv. Energy Mater. **10**, 2001445 (2020).

[37] T. B. Schon, B. T. McAllister, P.-F. Lia, and D. S. Seferos, The rise of organic electrode materials for energy storage, Chem. Soc. Rev. **45**, 6345 (2016).

[38] C. Caddeo and A. Mattoni, Atomistic investigation of the solubility of 3-alkylthiophene polymers in tetrahydrofuran solvent, Macromolecules **46**, 8003 (2013).

[39] T. Jarusuwannapoom, W. Hongroijanawiwat, S. Jitjaicham, L. Wannatong, M. Nithitanakul, C. Pattamaprom, P. Koombhongse, R. Rangkupan, and P. Supaphol, Effect of solvents on electro-spinnability of polystyrene solutions and morphological appearance of resulting electrospun polystyrene fibers, Eur. Polym. J. **41**, 409 (2005).

[40] L. P. Buchwalter, Chromium and tantalum adhesion to plasma-deposited silicon dioxide and silicon nitride, J. Adhes. Sci. Technol. **9**, 97 (1995).

[41] J. Vancea, G. Reiss, F. Schneider, K. Bauer, and H. Hoffmann, Substrate effects on the surface topography of evaporated gold films—A scanning tunnelling microscopy investigation, Surf. Sci. **218**, 108 (1989).

[42] V. Palermo, M. Palma, and P. Samorì, Electronic characterization of organic thin films by kelvin probe force microscopy, Adv. Mater. **18**, 145 (2006).

[43] H. Fan, S. Han, Z. Song, J. Yua, and H. E. Katz, Organic field-effect transistor gas sensor based on GO/PMMA hybrid dielectric for the enhancement of sensitivity and selectivity to ammonia, Org. Electron. **67**, 247 (2019).

[44] C. Reese and Z. Bao, Overestimation of the field-effect mobility via transconductance measurements and the origin of the output/transfer characteristic discrepancy in organic field-effect transistors, J. Appl. Phys. **105**, 024506 (2009).

[45] J. Artbauer, Electric strength of polymers, J. Phys. D: Appl. Phys. **29**, 446 (1996).

[46] X. Tang, C. Din, S. Yu, Y. Liu, H. Luo, D. Zhang, and S. Chen, Synthesis of dielectric polystyrene via one-step nitration reaction for large-scale energy storage, Chem. Eng. J. **446**, 137281 (2022).